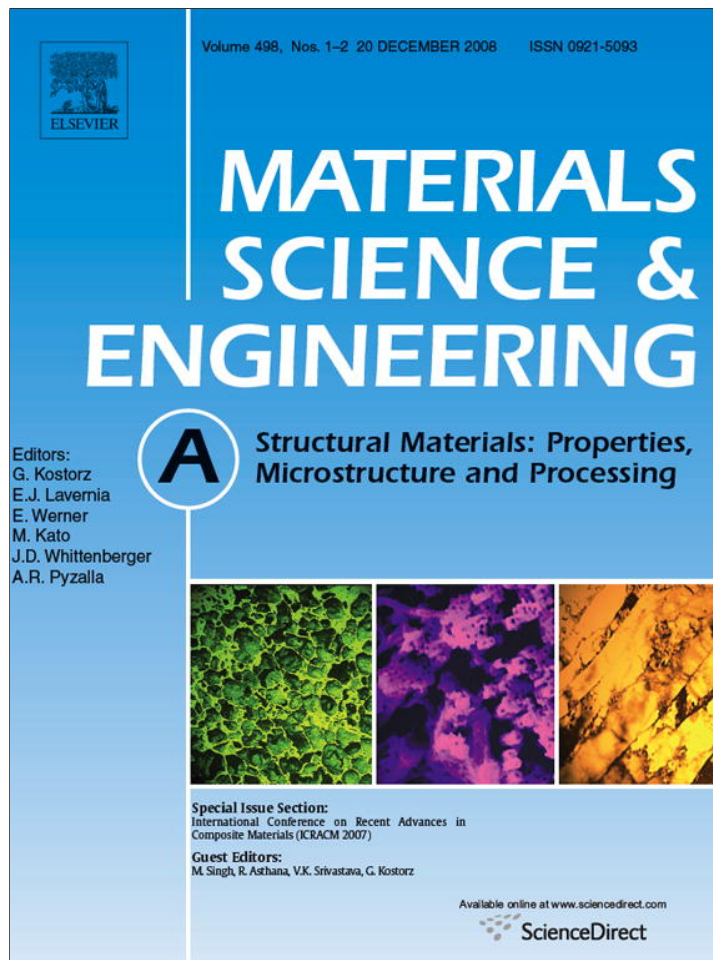


Provided for non-commercial research and education use.  
Not for reproduction, distribution or commercial use.



This article appeared in a journal published by Elsevier. The attached copy is furnished to the author for internal non-commercial research and education use, including for instruction at the authors institution and sharing with colleagues.

Other uses, including reproduction and distribution, or selling or licensing copies, or posting to personal, institutional or third party websites are prohibited.

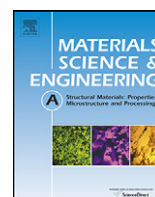
In most cases authors are permitted to post their version of the article (e.g. in Word or Tex form) to their personal website or institutional repository. Authors requiring further information regarding Elsevier's archiving and manuscript policies are encouraged to visit:

<http://www.elsevier.com/copyright>



Contents lists available at ScienceDirect

## Materials Science and Engineering A

journal homepage: [www.elsevier.com/locate/msea](http://www.elsevier.com/locate/msea)

## Neutron diffraction residual strain measurements in post-treated thermal spray cermet coatings

R. Ahmed<sup>a,\*</sup>, H. Yu<sup>a</sup>, V. Stoica<sup>a</sup>, L. Edwards<sup>b,c</sup>, J.R. Santisteban<sup>d</sup><sup>a</sup> Heriot-Watt University, School of Engineering and Physical Sciences, Edinburgh EH14 4AS, UK<sup>b</sup> The Open University, Department of Materials Engineering, Walton Hall, Milton Keynes MK7 6AA, UK<sup>c</sup> Institute of Materials Engineering, Australian Nuclear Science and Technology Organisation, PMB1, Menai NSW 2234, Australia<sup>d</sup> Rutherford Appleton Laboratory, ISIS, Didcot OX11 0QX, UK

## ARTICLE INFO

## Article history:

Received 11 February 2008

Received in revised form 22 June 2008

Accepted 17 August 2008

## Keywords:

Neutron diffraction  
Residual strain  
Thermal spray coating  
Delamination  
HIPing

## ABSTRACT

The aim of this investigation was to ascertain the relative changes in residual stress profile after the post-treatment of thermal spray WC–NiCrBSi coatings and relate these changes to the microstructural and tribo-mechanical properties. Residual strain measurements were performed using neutron diffraction technique in vertical scan mode. Functionally graded HVOF (JP5000) WC–NiCrBSi coatings were thermally sprayed on AISI 440C steel substrate discs, some of which were given different post-treatments i.e. HIPing at two different temperatures of 850 °C and 1200 °C, and heat-treatment in inert atmosphere at 1200 °C. Changes in microstructure due to heat-treatment were identified using SEM, XRD and light microscopy and correlated with tribo-mechanical properties determined using microhardness, Young's modulus and fatigue testing. It was found that whilst simple models based upon the differences in coefficient of thermal expansion can be adapted to predict the approximate average residual stresses after the post-treatment, refined models based upon microstructural change, substrate plasticity, influence of heating/cooling rate, and pressure during the post-treatment are necessary for the reliable prediction of residual stress fields. Such models may then be utilised to tailor the residual stress profile during the post-treatment for specific industrial applications. Improvement in coating fatigue performance was related to the attenuation of stress gradient within the coating layers, and to the homogenisation of stress profile at the coating substrate interface at the higher HIPing temperature of 1200 °C. The presence of isostatic pressure during the HIPing post-treatment produced a more uniform residual stress and Young's modulus profile, and hence a reduced stress concentrations that exacerbate fatigue failure.

© 2008 Elsevier B.V. All rights reserved.

## 1. Introduction

Ceramic particle reinforced sprayed coatings are finding increasing use within industry as they provide cost-effective, durable, and environmental friendly solutions to combat corrosive, erosive and fatigue failures. Whilst industrial demands push the use of thermal spray cermet coatings towards high stress impact resistance applications, durability and safety implications dictate that these coatings should resist delamination and spalling failure under very severe tribological conditions. A major factor dictating the resistance to fatigue and delamination failure in thermal spray coatings is the residual stress field within the coating and substrate material. Thermal spraying processes induce complex residual stress fields made up of combinations of the quenching (microtensile)

residual stresses produced at the splat level due to the very high cooling rates (e.g. 1000 K/ms for Ni) of individual lamellae, and the macro-compressive or tensile residual stresses due to the mismatch of the coefficient of thermal expansion (CTE) of the coating and substrate material. Fig. 1 summarises some of the influential factors dictating the residual stress state of thermal spray coatings. The influence of coating powder characteristics, coating process, and coating process parameters on the residual stress field has been the topic of research in many investigations [1–10], where experimental, mathematical and numerical approaches have been adapted to ascertain the generation of residual stress during coating deposition. Due to the difficulties in making conventional residual stress measurements of these coatings, there has been growing interest in the use of neutron diffraction [11–17], which has been applied to measure residual stresses profile in thicker thermal barrier coatings (TBCs) of zirconia, NiCrAlY and yttria stabilised zirconia. These investigations have provided very valuable information about the stress gradients, theoretical modelling of

\* Corresponding author. Tel.: +44 1314514722; fax: +44 1314513129.  
E-mail address: [R.Ahmed@hw.ac.uk](mailto:R.Ahmed@hw.ac.uk) (R. Ahmed).

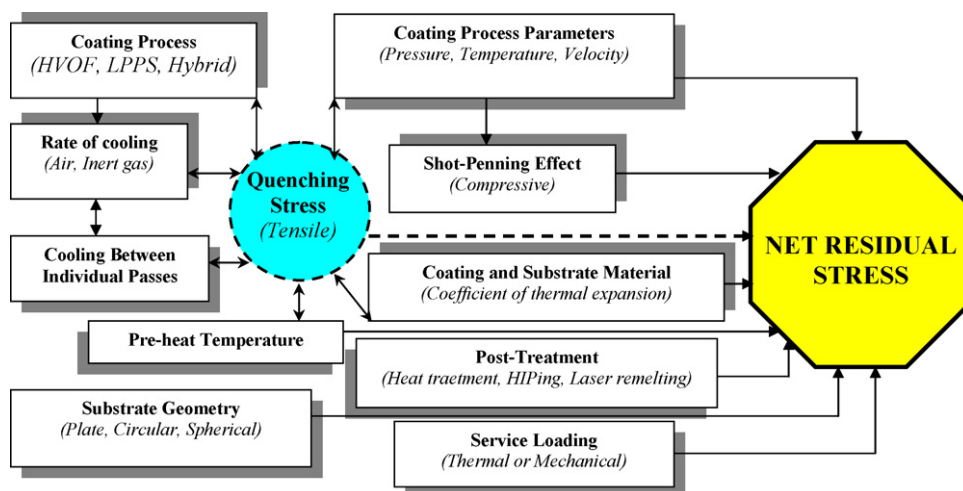


Fig. 1. Factors influencing the generation of residual stress in thermal spray coatings.

Table 1  
Coating and substrate materials

Powder	WC–10 wt.%NiCrSiBFeC	WC–40 wt.%NiCrSiBFeC
Particle size distribution ( $\mu\text{m}$ )	–45+15	–45+20
Apparent density ( $\text{g}/\text{cm}^3$ )	4.42	3.51
WC grain size ( $\mu\text{m}$ )	3–4	3–4
Powder manufacturing route	Agglomerated and sintered	Agglomerated and sintered
Powder shape	Spherical	Spherical
Alloy composition (wt.%)	Ni: Bal., Cr: 7.6, Si: 3.6, Fe: 2.4, B: 1.6, C: 0.25	Ni: Bal., Cr: 7.6, Si: 3.6, Fe: 2.4, B: 1.6, C: 0.25
Substrate	440C stainless steel	
Chemical composition (wt.%)	Fe: Bal., C: 0.86–1.20, Mn: 1.0max., Si: 1.0max., P: 0.04max., S: 0.03max., Mo: 0.75max., Cr: 16.0–18.0	

stress generation and their influence on coating performance of relatively thicker (typically 1000  $\mu\text{m}$  thick) thermal spray coatings.

Despite the fact that there have been several studies linking improvement in a coating's tribo-mechanical properties with coating post-treatment [18–24], investigations relating the changes in residual stress profile following post-treatments have been limited. This paper therefore aims to investigate the through thickness changes in the residual strain profile of relatively thin (400  $\mu\text{m}$ ) functionally graded WC–NiCrBSi coatings using neutron diffraction and relate these changes to the influence of coating post-treatment. Residual stress results from this investigation are then related to the previously reported delamination and fatigue resistance of these coatings [25].

## 2. Experimental test procedure

### 2.1. Coating preparation

Two compositions of spray dried and sintered WC–NiCrBSiFeC composite powders i.e. 10 wt.% Ni alloy, 90 wt.% WC and 40 wt.% Ni alloy, 60 wt.% WC were used in this investigation. The properties of these powders are listed in Table 1. The substrates were AISI 440C stainless steel discs of 31-mm diameter and 8-mm thickness. Prior to the coating deposition, a typical industrial methodology of grit blasting, cleaning, and then preheating was followed. High velocity oxy-fuel (HVOF) JP5000 spraying was carried out using the parameters industrially optimised for this material (Table 2). The first layer, WC–40 wt.%NiCrBSiFeC, was deposited onto the substrate to an approximate thickness of 100  $\mu\text{m}$ , and the second WC–10 wt.%NiCrSiFeBC layer

was subsequently applied to achieve a total as-sprayed coating thickness of approximately 500  $\mu\text{m}$ . Coatings were then ground and polished to achieve a total approximate thickness of 400  $\mu\text{m}$ .

### 2.2. Coating post-treatment

Two different post-treatments i.e. HIPing (hot isostatic pressing) and heat-treatment in inert atmosphere were considered in this investigation. The latter being used to investigate the influence of post-treatment pressure on coating's tribo-mechanical properties. The HIPing post-treatment was carried out for 1 h at a constant pressure (150 MPa) in argon environment. The coatings were not encapsulated and were HIPed at 850  $^{\circ}\text{C}$  and 1200  $^{\circ}\text{C}$ . The heat-treatment was carried out in an argon environment to prevent oxidation of the coating systems, at the higher temperature of 1200  $^{\circ}\text{C}$  for direct comparison with the HIPing post-treatment. The coated discs were placed in the furnace, which was evacuated of air, filled with argon and heated at 4  $^{\circ}\text{C}/\text{min}^{-1}$ . The coatings were held for 1 h at 1200  $^{\circ}\text{C}$  before being cooled at a rate of 4  $^{\circ}\text{C}/\text{min}^{-1}$  until 800  $^{\circ}\text{C}$ , and then allowed to cool naturally to room temperature.

Table 2  
Spraying parameters

Spray gun	JP5000
Oxygen flow ( $\text{l}/\text{min}$ )	8931
Kerosene flow ( $\text{l}/\text{min}$ )	0.321
Spraying distance (mm)	380
Spraying rate ( $\text{g}/\text{min}$ )	50

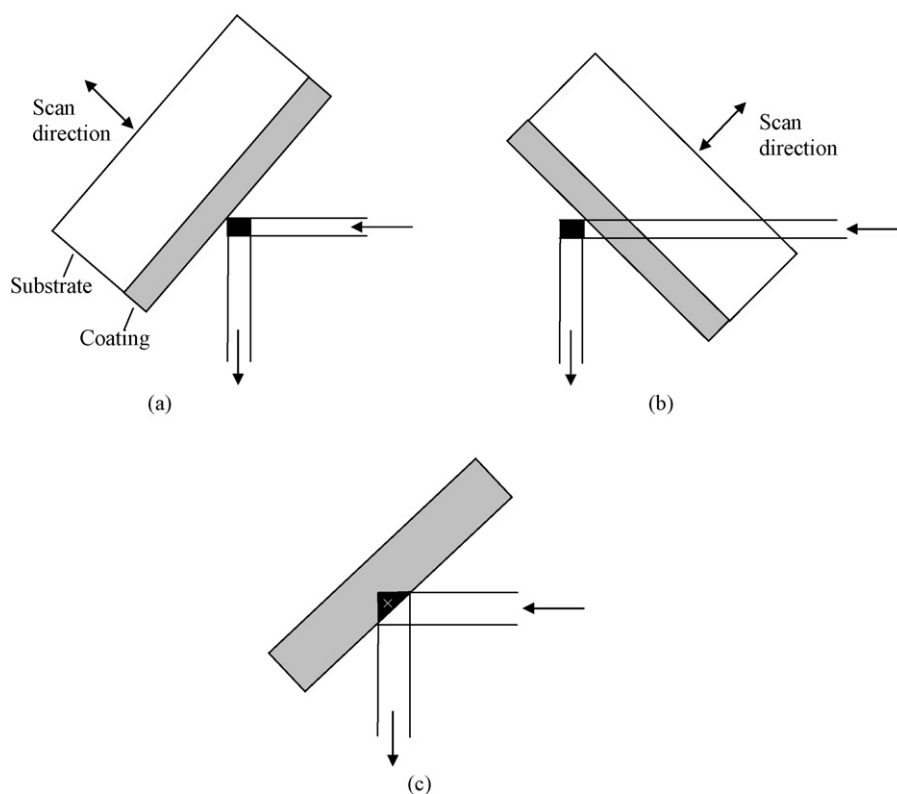


**Fig. 2.** Horizontal scan of the coated sample relative to the fixed gauge volume (a) in reflection mode to measure the strain component perpendicular to the surface and (b) in transmission mode to determine the in-plane strain component. Arrows indicate the scan directions and the path of neutrons. (c) Sample and gauge volume during the scan, when the gauge volume is only partially filled. Cross indicates the centre of gravity of gauge volume [15].

### 2.3. Neutron diffraction measurements

Neutron diffraction measurements were performed at ISIS (Rutherford Laboratory), UK using a dedicated strain measurement diffractometer (ENGIN-X) [26]. This is a pulsed neutron diffractometer equipped with slits and collimators to enable measurements from small gauge volumes. This instrument operates in a fundamentally different manner from most reactor-based instruments, as instead of measuring Bragg reflections by scanning a detector from low to high  $2\theta$ , ENGIN-X like its predecessor, ENGIN, uses a pulsed polychromatic beam to measure Bragg reflections at fixed scattering angles ( $2\theta=90^\circ$ ) using the time of flight of each diffracted neutron to characterise its wavelength [27].

There are three basic requirements for the accurate measurement of near-surface strains using neutron diffraction [28]. Firstly the position of the surface with respect to the neutron beam must be accurately known. This may be achieved by extremely careful optical alignments using theodolites or other optical instruments. Although accurate optical alignment of both the instrument and specimen is essential, determining the precise location of the specimen surface with respect to the incoming neutron beam is best achieved by fitting intensity variations measured by fast surface scanning to attenuation-based model of the resulting entrance curve. Using this method an alignment precision of better than 0.05 mm can be achieved [29].

Secondly, the 'centre of gravity', or centroid, of a near-surface gauge measurement volume must be calculated, as the centroid of the diffracting material clearly differs from the centre of the volume defined by the collimated neutron beam, as the latter volume straddles the specimen surface. It may also be necessary to consider the effects of attenuation for some materials as this may change the apparent position of the measurement centroid.

Finally, a correction may be required to allow for any pseudo-strain effects caused when the gauge volume straddles the surface or where the phase being measured is not homogeneously distributed within the gauge volume resulting in a changing diffraction geometry. This surface effect due to the changing diffraction geometry in the plane of diffraction is instrument-dependent and must be characterised for a given collimator and detector set-up.

Of the three essential requirements for precise near-surface measurement detailed above by far the most difficult and awkward to deal with are these pseudo-strains. These can be very large, often bigger than the physical strain in the component surface, and conventionally can only be dealt with by either a specific calibration measurement [13] or Monte Carlo type simulation of each measurement geometry used [30–34]. Furthermore, the magnitude of the effect is unique to each specimen and diffractometer used [28].

Previous work on the measurement of residual strains and stresses in thermal spray coatings reported by Scardi et al. [12], Matejicek et al. [13], Keller et al. [15] and Sampath et al. [16] used the conventional "horizontal scan" where the neutron beam illuminates the coating surface at  $45^\circ$  (Fig. 2). This technique, as just noted, produces inevitable systematic errors, which if not corrected, manifest as pseudo-strains because the "sample gauge volume", i.e., the intersection of the instrumental gauge volume (the black squares in Fig. 2) with the sample changes through the scan.

However, if the incident beam is scanned vertically out of a horizontal surface as shown in Fig. 3, there is no change in diffraction angle and, hence, no pseudo-strains generated as the gauge volume moves out of the surface [28,35]. So in the present work this vertical scan experimental arrangement was adopted as illustrated in Fig. 3. The coated specimen was moved up or down in the z-direction for depth profiling of strain in the coating and substrate materials. The incident beam was passed through a vertical and horizontal slit



steel substrate was measured at the near-surface of the substrate disc.

The direct elastic strain in the material at the measured direction can be calculated from the following expression:

$$\varepsilon = \frac{d - d_0}{d_0} \quad (1)$$

where  $d$  and  $d_0$  are the lattice parameter for the material and unstressed material, respectively. The elastic stress was calculated from these strain values using the reasonable assumption that the directions measured are the principal strain directions and using Hooke's law.

#### 2.4. Powder and coating characterisation

The X-ray diffraction (XRD) analysis was carried out using a Siemens D500 diffractometer with Cu K $\alpha$  (1.5406 Å, step size of 0.02° and dwell time of 2 s) radiations. The spray powders and the coatings were also characterised using a scanning electron microscope utilising secondary electron and energy-dispersive X-ray detectors. Microhardness measurements were carried out under a load of 2.94 N using a Vickers microhardness (Mitutoyo-Mvk-H1) test machine. Ten measurements were performed on each coating surface and thirty on each cross-section, which were distributed

in 3 lines of 10 measurement points each, at 50  $\mu\text{m}$ , 150  $\mu\text{m}$  and 250  $\mu\text{m}$ , respectively from the coating's surfaces. A distance of 100  $\mu\text{m}$  between all indentations was ensured to eliminate stress-field effects from nearby indentations.

Elastic modulus and fracture toughness tests were also performed via the indentation method. The indentation modulus was measured using real time displacement of the force indentation curve during a hardness test carried out under a load of 500 mN, and correlated to the Young's modulus using the following equation:

$$E = Y_{\text{HU}}(1 - \nu^2) \quad (2)$$

where  $Y_{\text{HU}}$  is the indentation modulus and  $\nu$  is the Poisson's ratio. Further details of this test method can be found in Buchmann et al. [36].

#### 2.5. Rolling contact fatigue (RCF) tests

In order to ascertain the delamination and fatigue resistance of thermal spray coatings test specimens were subjected to RCF tests. A modified four ball machine was used to study the RCF performance of coated rolling elements. The set-up of the test assembly comprised of the coated disc which was assembled to the drive shaft via a collet, and drove three planetary balls, which act as the thrust rolling elements in the configuration of the deep groove

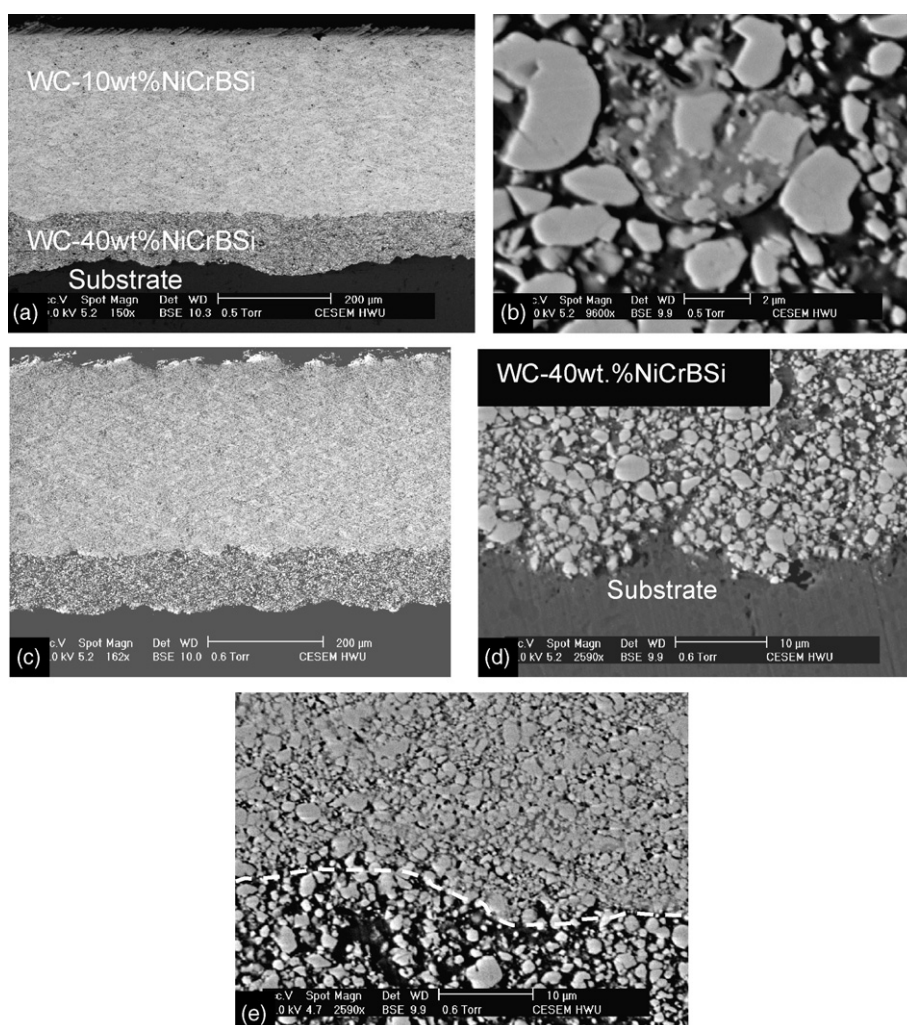


**Fig. 6.** SEM observations of the as-sprayed and HIPed at 850 °C coatings; (a) overall view of as-sprayed coating, (b) lower coating layer of the as-sprayed coating, (c) HIPed at 850 °C coating, (d) coating substrate interface of HIPed coating, (e) interface (indicated by broken line) of the top (WC-10 wt.%NiCrBSi) and bottom (WC-40 wt.%NiCrBSi) coating layers of the HIPed coating.

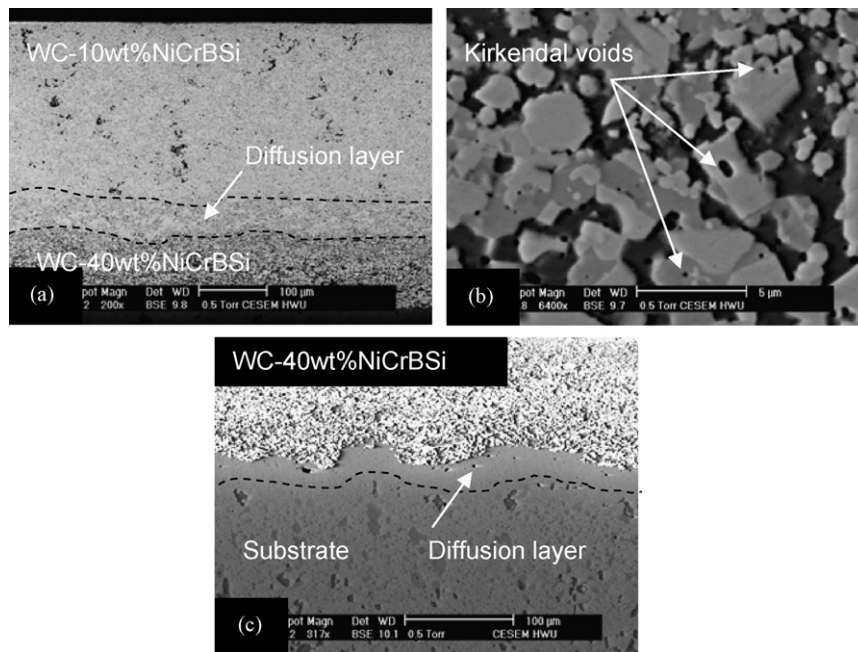


Fig. 7. SEM observations of the heat-treated and HIPed at 1200 °C coatings; (a) heat-treated coating indicating diffusion layer at the interface of two coating layers, (b) heat-treated coating indicating sintering of carbides in the bottom coating layer, (c) coating substrate interface of coating HIPed at 1200 °C indicating diffusion layer at the coating substrate interface.

ball bearing. RCF tests were conducted under immersed lubrication conditions at a spindle speed of  $4000 \pm 10$  rpm. Failure was defined as the increase in vibration amplitude above a pre-set level. Two test lubricants i.e. Hitec-174 and Exxon-2389 were used in the testing programme. Hitec-174 is a high viscosity hydrocarbon oil having a kinematic viscosity of  $200 \text{ mm}^2 \text{ s}^{-1}$  at  $40^\circ\text{C}$ . Exxon-2389 is a commercially available synthetic turbo-oil having a kinematic viscosity of  $12.4 \text{ mm}^2 \text{ s}^{-1}$  at  $40^\circ\text{C}$ . The ratio ( $\lambda$ ) of the elasto-hydrodynamic lubricant (EHL) film thickness to the average surface roughness was calculated as  $\lambda > 3$  and  $3 > \lambda > 1.5$  for the Hitec-174 and Exxon-2389 lubricants, respectively. Further details of the test method and ball kinematics can be obtained from Stewart et al. [25].

### 3. Experimental results

#### 3.1. Microstructural identification

##### 3.1.1. X-ray diffraction analysis

Fig. 5 shows XRD spectra of the top and bottom layers of the spray powder, as-sprayed, and post-treated coatings. Both layers had similar secondary phases, however the relative intensities were different due to the differences in the material composition. The main peaks were due to tungsten carbide (WC) for both compositions. As expected, higher intensities of these peaks were recorded for the WC-10 wt.% Ni alloy powder. Beside the carbide phase, the powder spectra revealed small amounts of metallic nickel and/or chromium. Additionally some chromium carbide ( $\text{Cr}_7\text{C}_3$ ) was also detected, a phase which is attributed to the transformations generated during the sintering stage of the powder. The microstructural phases observed in the coating HIPed at 1200 °C were very similar to that of the heat-treated coating and are, hence, are not presented here.

##### 3.1.2. SEM observations

Scanning electron micrographs of the as-sprayed and post-treated coatings are presented in Figs. 6 and 7. These figures show

the main features of the two coatings, highlighting the difference between them at higher magnifications. Fig. 6a and c shows an overall view of the as-sprayed and HIPed at 850 °C coatings. There were no significant differences between the morphology of these two coatings, hence only higher magnification images of one (HIPed at 850 °C) are shown in Fig. 6d and e. A clear distinct boundary could be observed both at the coating substrate interface and at the interface of two coating layers.

The SEM observations of the coating HIPed and heat-treated at 1200 °C were very similar in their morphology. Some observations are shown in Fig. 7 for both post-treatments. The main distinctions of post-treatment at this temperature from the as-sprayed and HIPed at 850 °C coatings were the formation of diffusion zones both at the coating substrate interface and at the interface of two layers. Agglomeration of carbides and formation of Kirkendal voids were also seen at this post-treatment temperature.

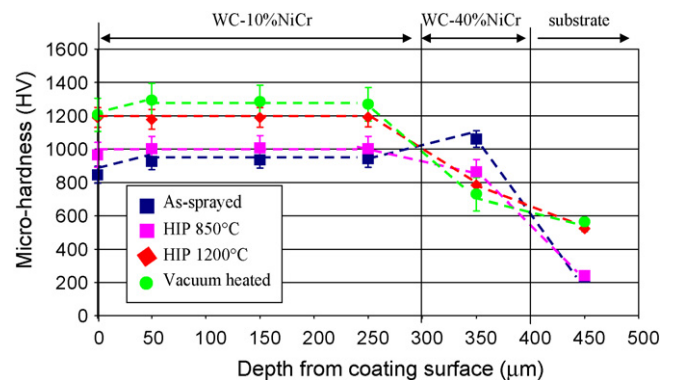


Fig. 8. Microhardness values for as-sprayed, HIPed at 850 °C, HIPed at 1200 °C and vacuum heated WC-NiCr functional graded coatings.

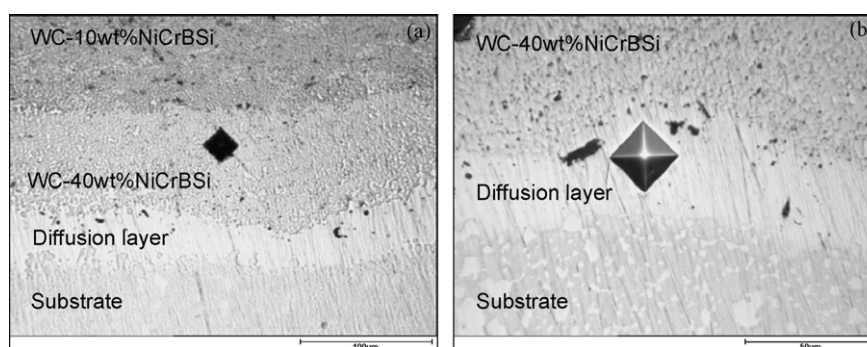


Fig. 9. Light microscope micrographs of (a) coating bottom layer and new layer and (b) indentations ( $HV_{100}$ ) performed on the new layer of the coating HIPed at  $1200^{\circ}\text{C}$ .

### 3.2. Mechanical testing

#### 3.2.1. Microhardness measurements

The results of the microhardness measurements are presented in Fig. 8. The hardness values quoted are an average of 30 measurements which were performed on the coating surface, and on five lines distributed along the cross-section. In order to measure the hardness of the diffusion layer formed inside the coating's bottom layer a lower load of 100 g was used to allow indentation inside the layer. The micrograph presented in Fig. 9a shows the morphology of the new-formed diffusion layer in comparison to the substrate and the coating layers. Fig. 9b indicates the location of the indentation performed on the diffusion layer. Fig. 10 shows a decrease in the substrate microhardness approaching the coating/substrate interface. The results suggest that the treatment carried out at  $1200^{\circ}\text{C}$  produced softening of the coating bottom layer in the vicinity of the interface ( $\sim 30\ \mu\text{m}$ ).

#### 3.2.2. Indentation modulus measurements

Fig. 11 shows the results of both surface and through thickness indentation modulus measurements in the as-sprayed and post-treated coatings. The measurements carried out on the heat-treated coating gave an unexpected trend. The bottom layer of the heat-treated coating had a lower indentation modulus than the bottom layer of the as-sprayed coating. However, for the rest of the measurements, significantly higher modulus values were measured. The highest increase was measured on the coating's surface where a high average value of about 480 GPa was measured, which is similar to that of sintered WC-Co, and indicates high degree of localised sintering in the near-surface region of the heat-treated coating.

#### 3.3. Residual stress and strain measurements via neutron

Fig. 12 presents the residual strain measurement results obtained using the neutron diffraction technique. These results

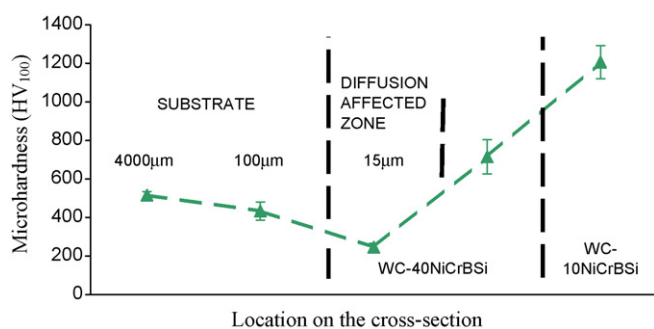


Fig. 10. Microhardness results ( $HV_{100}$ ) on the coating HIPed at  $1200^{\circ}\text{C}$ .

indicate that the average coating and substrate strain varies significantly with post-treatment. Stress values calculated from the strains using the measured Young's modulus values and an equibiaxial plane stress assumption are also given in the same figure. An average value of Young's modulus was used where measurement depth of residual strain and indentation modulus measurements did not match. Young's modulus values were converted from indentation modulus values (Eq. (2)) on the basis of approximate Poisson's ratio of the coating layers. Although the exact value of Poisson's ratio was not measured, it has been suggested that the Poisson's ratio of thermal spray deposits is generally much lower than that of the bulk material [9,37]. However, there is also some evidence indicating that in the case of ceramics, e.g. partially stabilised plasma sprayed zirconia, the Poisson's ratio of the deposits is not different from bulk material [38]. The residual stress values presented in Fig. 12 were based upon an approximate Poisson's ratio of 0.22, which was based upon the value for WC, which was the main constituent of the coating layers. However, it should be noted that the calculated stress values were not very sensitive to the value of Poisson's ratio used e.g. stress values vary by a maximum of 5% if lower bound values of Poisson's ratio (e.g. 0.05) is used. Furthermore, the relative ranking of stress values for different post-treatments will remain the same.

#### 3.4. Rolling contact fatigue

Previous investigations [25] on the RCF behaviour of these coatings have indicated a strong dependence of post-treatment on the RCF performance. Some of these results are reproduced here to aid discussion. Fig. 13 shows the RCF performance results of these coatings tested under a variety of tribological conditions of contact stress (2–2.7 GPa), contact configuration (conventional steel and

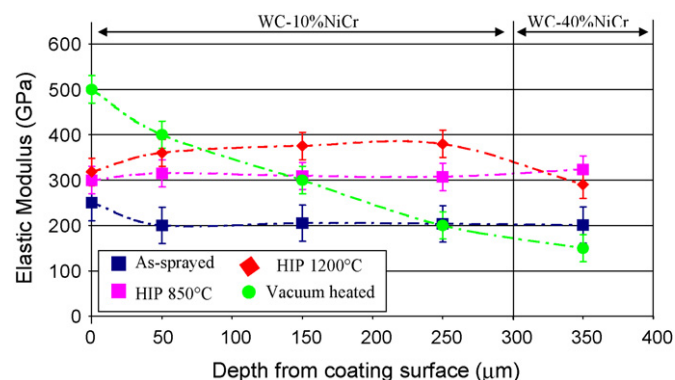


Fig. 11. Indentation modulus values for as-sprayed, HIPed at  $850^{\circ}\text{C}$ , HIPed at  $1200^{\circ}\text{C}$  and vacuum heated WC-NiCr functional graded coatings.

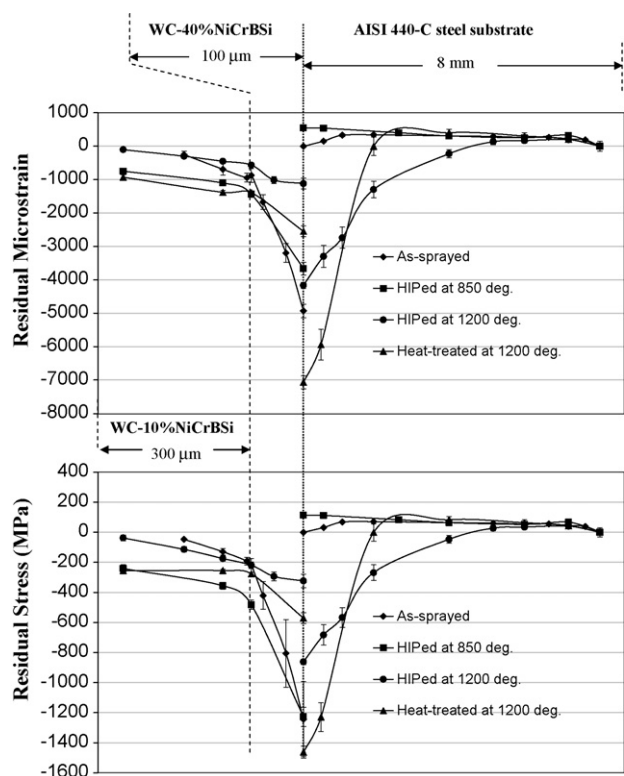


Fig. 12. Results of residual strain and stress obtained via neutron diffraction technique for the as-sprayed and post-treated thermal spray WC-NiCrBSi functionally graded coatings.

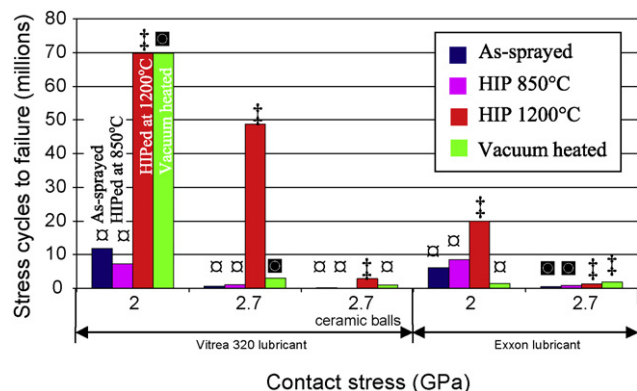


Fig. 13. Rolling contact fatigue results for as-sprayed, HIPed at 850 °C, HIPed at 1200 °C and vacuum heated coatings (failure modes—□ delamination; ■ spalling; † surface distress) [25].

hybrid ceramic), and lubrication regime (full film EHL with Vitrea 320 lubricant and mixed EHL regime with Exxon-2389 lubricant). Three distinct failure modes i.e. delamination, spalling and surface distress were observed in these coatings. All of these results indicate that the higher temperature post-treatment of 1200 °C had a more pronounced influence on the RCF performance of thermally sprayed WC-NiCrBSi coatings, with HIPing post-treatment outclassing the vacuum heated performance.

## 4. Discussion

### 4.1. Coating microstructure and microhardness

There have been several studies relating to the microstructure and structure–property relationships of thermal spray coatings

[39–41]. The aim of the discussion below is to highlight differences in the microstructure after the post-treatments, with a view to understand the residual strain and fatigue/delamination resistance.

#### 4.1.1. As-sprayed coatings

The microstructure of the as-sprayed coatings in the present study was typical of the lamella morphology associated with thermal spray coating process. The SEM observations indicate distinct boundaries at the interface of two coating layers and at the coating substrate interface (Fig. 6a), suggesting it is the mechanical interlock of splats that provides most of the bonding mechanism during coating deposition. The XRD patterns of the as-sprayed layers (Fig. 5a) indicate phase transformations during powder deposition. Several reflections indicate thermal decomposition of the carbides with formation of secondary tungsten carbide ( $W_2C$ ) and metallic tungsten (W), the latter overlapping the secondary tungsten carbide phase at  $2\theta$  of approximately  $40^\circ$ . The rim of brighter matrix phase indicating these changes can be observed in Fig. 6b. These changes are typical of the decomposition of WC-cermet coatings which occur from two sources as previously suggested e.g. by Lovelock [39] and Verdon et al. [40]. Firstly, the loss of carbon in the form of  $CO_2$ , and secondly the formation of amorphous/nano-crystalline phases through WC solubility in the matrix resulting in the formation of a nano-crystalline binder phase due to rapid cooling during deposition. These two mechanisms led to the decomposition of WC into W,  $W_2C$  and formation of amorphous regions which are seen in the X-ray diffraction pattern typically at a  $2\theta$  of approximately  $40^\circ$ .

#### 4.1.2. HIPed at 850 °C coatings

The SEM observations of the coating HIPed at 850 °C show a microstructure which is very similar to that of the as-sprayed coatings. The XRD patterns, however, show evidence of changes at the atomic level with phase transformations suggesting recrystallisation of some of the nano-crystalline/amorphous phase seen in the as-sprayed coatings and the formation of additional secondary phases ( $Cr_{23}C_6$  and  $Ni_2W_4C$ ). These phase changes were typical of the microstructural transformations associated with the amorphous to crystalline phases in the temperature range of 600–850 °C for WC-cermet coatings as reported by Nertz et al. [41], which resulted in an improvement in the coating's microhardness. In addition, although not appreciated through SEM observations, the process of sintering and diffusion of elemental species also occurred which improved the mechanism of splat bonding from mechanical interlock to metallurgical bonding, as seen in the modulus measurements (Fig. 11).

#### 4.1.3. Heat-treated and HIPed at 1200 °C coatings

The microstructural changes associated with the higher post-treatment temperature of 1200 °C were very similar for the HIPed and heat-treated coatings. The XRD results indicate formation of additional carbide and secondary phases ( $FeW_3C$ ,  $Fe_6W_6C$ ,  $Cr_7C_3$ ,  $Cr_3C_2$ ,  $NiB_2$ ,  $Ni_4B_3$ ). These phase changes resulted in an increase in hardness for both post-treatments. The nano-crystalline phase which was partially crystallised at 850 °C also fully crystallised. This meant that the nano-crystalline phase which surrounded the WC-particles (Fig. 6b) no longer exists (Fig. 7b).

The SEM investigations (Fig. 7) indicated that these changes were accompanied by the formation of diffusion layers both at the coating substrate interface and at the interface of two layers. The SEM observations indicate that no carbides are formed in this diffused layer, which was further confirmed by the lower hardness of the diffusion layer (Figs. 9 and 10). The diffusion layer therefore represents a solid solution of the diffused species. The different rates of diffusion also resulted in the formation of the Kirkendall voids

(Fig. 7b). The WC grains also interact with the matrix at this post-treatment temperature which initiates dissolution in the Ni-rich matrix along with the sintering of carbides (Fig. 7b). The extent of this dissolution was governed by the solubility of WC in the matrix components which bring about a decrease in the activation energy for atomic movement across the carbide boundaries. Such mechanisms have previously been reported by Meredith and Milner [42] and Ryoo et al. [43] and indicate that the movement of carbide interfaces ceases when low energy prismatic carbide interfaces form. Further details of these changes are described in Stoica [44]. The phase transformation within the newly formed diffusion zones were also analysed by neutron diffraction. Analysis using X-ray diffraction was not possible due to the lack of a mechanism of precise layer removal. Neutron diffraction analysis indicated the presence of  $\text{FeW}_3\text{C}$  (Fig. 4) within the diffusion zone at the coating substrate interface, which resulted from the diffusion of Fe from the substrate. The diffusion of elemental species i.e. Ni and C from the coating and Fe and Cr from the substrate into the diffusion zone was further verified by electron probe microscopy analysis (EPMA) mapping of the coating cross-sections.

#### 4.2. Indentation modulus and coating anisotropy

Indentation modulus measurements of the as-sprayed coatings indicate an average value of 200 GPa in the top layer (Fig. 11). This is typical of WC-cermet coatings where the Young's modulus of deposits is expected to range between 30 and 40% of the bulk material value [9,37]. The modulus value is slightly higher on the surface than in the cross-section, which is indicative of the anisotropy seen in thermal spray coatings [45,46]. This is mainly due to the preferred orientation of microcracks and defects between lamellas, which are generally parallel to the coating substrate interface. The diffusion layers formed after the post-treatment, especially at the higher temperature indicate that metallurgical bonding was established between the splats, thereby increasing the indentation modulus of coatings after the post-treatment. The extent of this change was a function of post-treatment temperature for the HIPed coatings, whereas a non-homogenous change through the coating section was observed in the case of heated-treated coatings. This non-homogenous trend in the elastic modulus was caused by the absence of isotatic pressure during this post-treatment, and indicated that the sintering caused under the influence of HIPing pressure was more uniform across the coating section. The increase in the modulus values after the HIPing post-treatment was far greater in the coating cross-section than on the coating surface. This further indicates that preferential sintering occurred at the interface of lamellas under the presence of isotatic pressure. In the absence of this pressure, the sintering process results in variability in the coating's modulus with heat-treatment (Fig. 11).

The ratio of modulus value ( $E_s/E_x$ ), measured on coating surface ( $E_s$ ) to the average through thickness value of modulus in the top layer of coating's cross-section ( $E_x$ ), gives an indication of the anisotropic nature of thermal spray coatings. These anisotropy values for the as-sprayed, HIPed at 850 °C, HIPed at 1200 °C and heat-treated coatings are approximately 1.3, 0.93, 0.85 and 2, respectively. Previous investigations have indicated that for the case of as-sprayed WC-cermet coatings the Young's modulus anisotropy could be as high as 2, whereas for the case of ceramics the anisotropy was measured as around 1.3 on the basis of plan-section and cross-section modulus measurements [46]. Furthermore, for the case of TBCs, the thermal exposure reduces this anisotropic behaviour due to preferred sintering at the intersplat boundaries. A similar reduction in anisotropic behaviour was also observed for the case of HIPed coatings. However for the case of heat-treated coatings, the anisotropy was much higher than that observed in the case

of as-sprayed coatings, which was mainly due to the non-uniform sintering in the coating cross-section. Hence, it can be appreciated that although the phase composition, hardness and morphology of the coating in terms of diffusion layers at the interface of two coating layers, and also at the coating substrate interface were very similar for the case of heat-treated and HIPed at 1200 °C coatings, the presence of isotatic pressure was significant in homogenising sintering at the splat boundaries, thereby influencing the modulus measurements for the two post-treatments at 1200 °C.

#### 4.3. Residual stress and strain distribution

The measurements show that the strain and calculated stress in both the coating layers was compressive, whereas it varied from tension to compression within the substrate after the post-treatment temperature at the higher temperature of 1200 °C. In the case of as-sprayed coating, or post-treated coating at the lower temperature of 850 °C, the residual stress in the substrate was tensile. The compressive nature of residual stress in the coating layers was predominantly due to the higher coefficient of thermal expansion of the substrate material (Fig. 1).

##### 4.3.1. As-sprayed residual strain and stress profile

In the case of the as-sprayed coating, the strain and calculated stress in the top layer was compressive but the stress gradient was lower than that of the lower layer. In the bottom layer, however, the stress gradient was much higher with a sharp variation in the stress field at the coating substrate interface. These stress values illustrate the combined effect of the three main sources of stress generation i.e. two sources of compressive stress via thermal mismatch and a peening effect due to the high particle velocity of JP5000 spraying, and a third source of tensile residual stress due to quenching of lamellas (Fig. 1). The stress in the near-surface region is less compressive than the underlying coating material, which is indicative of the influence of quenching stress and absence of a peening effect of the top most coating layer. If the coating thickness is increased beyond a critical value, the stress may become tensile in the near-surface region. Previous research has also indicated that the residual stress distribution in the as-sprayed thermal spray cermet coatings can vary from tensile in the near-surface region to compressive near the coating substrate interface [1,6]. It is, therefore, not surprising that thicker cermet coatings delaminate relatively easily due to this stress gradient as it leads to a high bending moment within the deposit or at the coating substrate interface [13]. At the coating substrate interface, the discontinuity in the stress field is typical of overlay coatings, which is due to the mismatch of thermal and mechanical properties of the coating and substrate material. Within the substrate material, however, the residual stress at the coating substrate interface is close to zero with a small gradient of tensile stress through its thickness. These low values of tensile residual stress are indicative of the low substrate heating during thermal spraying. The near zero value of residual stress within the substrate at the coating substrate interface, instead of the expected tensile stress is indicative of the influence of compressive residual stress due to grit-blasting prior to thermal spraying, which was attenuated due to the differences in the CTE during the coating process.

##### 4.3.2. Residual stress in the post-treated coatings

In the case of post-treated coatings, the stress generation was mainly controlled by the differences in the CTE of the coating and substrate materials. Gill [9] has indicated that that the CTE of sprayed materials do not differ greatly from those of bulk materials. Furthermore, in the case of cermets a linear rule of mixtures can be applied to approximate the CTE of the WC–10 wt.%NiCrBSi and

WC–40 wt.%NiCrBSi coatings as  $6 \times 10^{-6} \text{ K}^{-1}$  and  $8.3 \times 10^{-6} \text{ K}^{-1}$ , respectively. This methodology for approximating the CTE can be verified by applying it to the case of WC–20 wt.%Co coatings, where the linear rule indicates a value of  $6.9 \times 10^{-6} \text{ K}^{-1}$ . The experimentally measured CTE value for this coating material is  $7.4 \times 10^{-6} \text{ K}^{-1}$  [37], which is not significantly different as first approximation. The CTE value for the substrate material was  $10.2 \times 10^{-6} \text{ K}^{-1}$ . In order to estimate the generation of residual stress due to thermal mismatch, Matejcek et al. [13] has indicated that the stress gradient can be numerically computed by considering the variation in CTE values with temperature. They used experimentally measured variation in CTE vs. temperature to compute (via a Multitherm calculation) the residual stress gradient in NiCrAlY coating, annealed at  $650^\circ\text{C}$ . Although such calculations and models are necessary to predict the through thickness residual stress profile in the coated specimen, Gill [9] has indicated that simple elastic analysis of the in-plane thermal stresses produced in a thin coating attached to a thick substrate can be approximated by:

$$\sigma_d = E_d \Delta T (\alpha_s - \alpha_d) \quad (3)$$

where  $\sigma_d$  is the stress in the deposit,  $E_d$  is the Young modulus of the deposit,  $\Delta T$  change in temperature, and  $(\alpha_s - \alpha_d)$  represents the difference in the CTE of the deposit and underlying substrate. If this methodology is adapted to estimate average stress in the top/bottom coating layers in the present work, stress values of  $-600 \text{ MPa}/-478 \text{ MPa}$  and  $-840 \text{ MPa}/-675 \text{ MPa}$  are predicted for the case of post-treatment temperatures of  $850^\circ\text{C}$  and  $1200^\circ\text{C}$ , respectively. A slightly refined approach of predicting average residual stress due to the differences in CTE can also be adapted here on the basis of a composite beam analysis. In this approach a composite beam of three materials i.e. substrate, bottom coating layer and top coating layer can be assumed as perfectly adhered to each other. As the beam is in equilibrium, the sum of forces in the three materials must be zero, i.e.

$$\Sigma E_{t,b,s} A_{t,b,s} \left( \frac{x}{l} - \alpha_{t,b,s} \Delta T \right) = 0 \quad (4)$$

where<sup>1</sup>  $E$ ,  $A$  and  $\alpha$  represent the Young's modulus, cross-sectional area and CTE of the top, bottom and substrate materials. The term  $x/l$  represents the net strain in the beam due to constrained contraction and  $\Delta T$  represents the temperature change. Based upon this analysis, the net strain in the composite beam system can be evaluated and related to stress ( $\sigma$ ) using the equation:

$$\sigma_{t,b,s} = E_{t,b,s} \left( \frac{x}{l} - \alpha_{t,b,s} \Delta T \right) \quad (5)$$

Although the specimens in the current investigation were circular, the above analysis indicates that if a rectangular beam was used in analysis its length ( $l$ ) becomes irrelevant, as the relative term of strain ( $x/l$ ) is used here. The thickness of each material in the beam can be assumed to be the same as that of the coated specimen. The width of the beam can be approximated as 10 mm (as per gauge volume dimensions) as a first approximation. Based upon this analysis the average residual stress in the top/bottom/substrate materials can be approximated as  $-1741 \text{ MPa}/-560 \text{ MPa}/+81 \text{ MPa}$  and  $-1091 \text{ MPa}/-428 \text{ MPa}/+35 \text{ MPa}$  for the case of cooling from  $850^\circ\text{C}$  and  $1200^\circ\text{C}$ , respectively. It is worth noting that although these residual stress values are sensitive to the approximate beam width, the relative values of residual stress in the top layer, bottom layer and substrate materials will be un-effected.

The analysis based upon the above Eqs. (3) and (5) provide an estimate of the expected average residual stress values after the post-treatment. The experimentally measured average compressive stress values in the top/bottom layers for the cases of HIPing at  $850^\circ\text{C}$  and  $1200^\circ\text{C}$  are  $-341 \text{ MPa}/-1166 \text{ MPa}$  and  $-129 \text{ MPa}/-265 \text{ MPa}$ , respectively and for the case of heat-treated coatings, the averaged experimental values are  $-250 \text{ MPa}/-543 \text{ MPa}$ . Although the averaged experimental values in both layers are of the same order of magnitude as the theoretically approximated values (using Eqs. (2) and (4)), there are two features which do not fit the profile. Firstly, the stress in the case of higher post-treatment temperature of  $1200^\circ\text{C}$  should have been higher than that for the  $850^\circ\text{C}$ . However, the experimental results are contrary. Secondly, the stress in the lower layer should have been lower than that of the top layer as the difference in the CTE mismatch of the bottom layer and substrate is lower than that of the top and bottom coating layer.

There are four factors responsible for these differences in behaviour. Firstly the composition effect especially for the lower coating layer. In the top WC–10 wt.%NiCrBSi coating layer, where the volume fraction of carbides is five times the NiCrBSi matrix, the gauge volume is assumed to represent the macro-stress in the top coating layer i.e. neglecting the influence of micro-stress caused by the difference in CTE of the carbide-matrix system. This difference in volume fraction was however insignificant in the lower WC–40 wt.%NiCrBSi coating layer, and hence the influence of micro-stress caused by the difference in CTE's of the carbide and matrix phase will have a significant influence on the net residual stress in the lower coating layer. In the current measurement set-up, this micro-stress is not considered as only the stress in WC is measured. Hence, although the relative changes in the residual stress in the lower layer will not be influenced by the measurement technique, which was the aim of this investigation, and indicates significant influence of the post-treatment on the relative changes of residual stress, the stress measured is however not the absolute stress in the lower coating layer. Secondly, the geometrical effects i.e. the substrate is quite thick in comparison to the two coating layers, hence an approximation on the basis of single layer material (Eq. (3)) or multiple layers perfectly adhered (Eq. (5)) may not be valid. Free contraction of the bottom-coating layer is therefore constrained by the contraction of the top layer due to the differences in CTE, which induces more than expected stress gradient in it. Thirdly, there is diffusion at the interface of the top/bottom layers and at the coating substrate interface. These diffusion zones along with the introduction of phase changes within the coating material further complicate the stress field. These diffusion zones significantly influence the residual stress profile at the interface of layers e.g. the residual stress in the substrate near the interface is more tensile in the HIPed at  $850^\circ\text{C}$  post-treatment, than the as-sprayed layer, whereas the stress in this region is compressive after the post-treatment at higher temperature of  $1200^\circ\text{C}$ . Fourthly, the rate of cooling/heating during the post-treatment can significantly influence the residual stress or strain profile, which is not considered in the model. Additional factors such as plasticity at higher temperatures and thermal cycling effect of heat-treatment further influence the net residual stress profile. The influence of isostatic pressure during HIPing adds another variable, as it results in a more uniform stress distribution when compared to heat-treated coating at the same temperature. Similarly, existing model only considers the coating layer as a continuum material, and hence only able to predict macro-stress. Further numerical models are therefore necessary to predict the generation of residual stress profile in post-treated functional graded coatings at both micro- and macro-stress levels. These numerical models may also help integrate existing models of stress generation in as-sprayed thermal spray coatings

<sup>1</sup> Subscripts t, b and s relate to the materials properties for the top coating layer, bottom coating layer, and substrate, respectively.

where the generation of residual stress is mainly dictated by the coating process parameters for a given coating substrate system.

#### 4.4. Influence of residual stress on fatigue and delamination resistance

There are two important features of the through thickness neutron diffraction residual stress and strain measurements which provide valuable insight into the fatigue performance of these coatings. Firstly in the top WC–10 wt.%NiCrBSi layer, the level of compressive residual stress increases in the HIPed at 850 °C and heat-treated at 1200 °C coatings, whereas the level of compressive residual stress attenuates in the top HIPed at 1200 °C layer. Secondly in the lower coating layer and its interface with the substrate material, the residual stress gradient, which can lead to stress concentration and thus crack initiation and propagation, decreases after all post-treatments. However, the stress gradient due to the mismatch of the materials at the coating substrate interface and also at the interface of the two coating layers was minimised after HIPing at 1200 °C. The stress concentrations at the interface of materials, and high stress gradients within a coating layer can exacerbate the initiation and propagation of fatigue cracks. Considering the changes in the residual stress profile after all post-treatments, in which the stress gradient and mismatch was attenuated, the extent of which was dependent upon post-treatment conditions, it is not surprising that tests indicate significant improvements in RCF performance after post-treatment, especially at the higher stress level of 2.7 GPa (Fig. 13). The relative improvement in the RCF life was, however, very dependent upon the residual stress field and thus the post-treatment method and conditions, so that HIPing at 1200 °C results in the best relative performance.

Previous studies [47,48] on the delamination/spalling behaviour of thermally sprayed cermet coatings have indicated that although the depth of failure after delamination can generally be related to the depth of the cyclic orthogonal or maximum shear stress, crack initiation generally takes place at other stress concentration sites e.g. interfaces with a large mismatch of material properties and/or areas that see large stress gradients. In the case of the current functionally graded coatings, these stress sites were at the two interfaces i.e. between the top and bottom layer and the coating substrate interface, and high stress gradient in the bottom layer for all cases except HIPed at 1200 °C coatings. The residual stress distribution at these points is therefore critical in combating crack initiation and propagation for delamination failure. Although compressive residual stress values are thought beneficial to combat fatigue and delamination failure, too high compressive stress can also lead to premature delamination and fatigue failure. Hence, a relatively lower value of compressive residual stress, coupled with a uniform transition of stress field at the interface of two layers and at the coating substrate interface result in the superior RCF performance of HIPed at 1200 °C coatings.

In addition to the changes in coating performance, the failure mode of these coatings was significantly influenced by the residual stress profile, where delamination was seen as the most common failure mode in the as-sprayed, HIPed at 850 °C, and heat-treated coatings. Delamination in thermal spray coatings is a catastrophic failure mode where large portions of coating detach from substrate resulting in sheet like debris [47,48]. However, the failure mode in the HIPed at 1200 °C coatings was surface distress which is neither catastrophic nor instantaneous but progressive. Although a number of factors including coating thickness, contact stress, lubrication, contact configuration and residual stress profile influence delamination failure, the changes in failure mode in this case were principally dependent upon the residual stress differences as other factors were similar for the coatings under consideration.

## 5. Conclusions

1. Residual stress measurements via neutron diffraction analysis indicate that relative attenuation of stress gradient within and at the interface of coating layers was responsible for the improvement in fatigue performance after the post-treatment.
2. Changes in residual stress profile following the post-treatment were influenced by the post-treatment temperature and pressure, where presence of isostatic pressure during HIPing provides a more uniform residual stress gradient when compared to conventional heat-treatment. Simple models based upon the differences in the CTE can provide an indication of the expected residual stress field as a first approximation; however more detailed models are necessary to incorporate the influence of heating/cooling rates, influence of pressure, plasticity and phase transformations during the post-treatment.
3. Intersplat bonding improves after the coating post-treatment which was reflected by the changes in coating elasticity. The extent of these changes was a function of both post-treatment temperature and pressure.
4. Microstructural investigations indicate phase transformations within both coating layers and within the substrate at the higher post-treatment temperature of 1200 °C.

## Acknowledgements

Authors would like to acknowledge the support of ISIS (grant number RB15141) for neutron diffraction measurements. They would like to thank Dr Susan Davies at Bodycote HIP Ltd., UK for her support during the HIPing post-treatment.

## References

- [1] D.J. Greving, E.F. Rybicki, J.R. Shadley, *Journal of Thermal Spray Technology* 3 (1994) 379–388.
- [2] H. Gassot, T. Junquera, V. Ji, M. Jeandin, V. Guipont, C. Coddet, C. Varney, L. Grandsire, *Surface Engineering* 17 (2001) 317–322.
- [3] R.T.R. McGrann, D.J. Greving, J.R. Shadley, E.F. Rybicki, B.E. Bodger, D.A. Somerville, *Journal of Thermal Spray Technology* 7 (1998) 546–552.
- [4] J. Matejcek, S. Sampath, S. Dubsy, *Journal of Thermal Spray Technology* 7 (1998) 489–496.
- [5] J. Stokes, L. Looney, *Surface and Coatings Technology* 177 (2004) 18–23.
- [6] M. Buchmann, R. Gadow, J. Tabellion, *Materials Science and Engineering A* 288 (2000) 154–159.
- [7] R. Ahmed, M. Hadfield, *Wear* 209 (1997) 84–95.
- [8] R.T.R. McGrann, D.J. Greving, J.R. Shadley, E.F. Rybicki, T.L. Kruecke, B.E. Bodger, *Surface and Coatings Technology* 108–109 (1998) 59–64.
- [9] S.C. Gill, *Residual stress in plasma sprayed deposits*, PhD Thesis, Gonville and Caius College, Cambridge University, UK, 1993.
- [10] J. Matejcek, *Processing effects on residual stress and related properties of thermally sprayed coatings*, PhD Thesis, Materials Science and Engineering State University of New York, Stony Brook, NY, USA, 1999.
- [11] O. Kesler, J. Matejcek, S. Sampath, S. Suresh, Gnaeupel-Herold, T.P. Brand, H.J. Prask, *Materials Science and Engineering A* 257 (1998) 215–224.
- [12] P. Scardi, M. Leoni, L. Bertini, L. Bertamini, F. Crenuschi, *Surface and Coatings Technology* 108–109 (1998) 93–98.
- [13] J. Matejcek, S. Sampath, P.C. Brand, H.J. Prask, *Acta Materialia* 47 (2) (1999) 607–617.
- [14] F. Turquier, M. Ceretti, P. Hairry, I. Titeux, A. Lodini, *Physica B* 276–278 (2000) 872–873.
- [15] T. Keller, N. Margadant, T. Pirling, M.J.R. Escrivano, W. Wagner, *Materials Science Engineering A* 373 (2004) 33–44.
- [16] S. Sampath, X.Y. Jiang, J. Matejcek, L. Prchlik, A. Kulkarni, A. Viadva, *Materials Science Engineering A* 364 (2004) 216–231.
- [17] N. Markocsan, N. Nysten, P. Fogarassy, A. Manescu, *Proceedings of the ITSC-2004*, Osaka, Japan, ISBN0871708094, 2004, pp. 101–106.
- [18] W. Lenling, M.F. Smith, J.A. Henfling, *Beneficial effects of austempering post-treatment on tungsten carbide based wear coatings*, National Thermal Spray Conference, Long Beach, USA, ISBN 0871703920, 1990, pp. 227–232.
- [19] P.K. Ghosh, et al., *International Journal of Joining Materials* 9 (3) (1997) 114–121.
- [20] R. Ahmed, H. Yu, S. Stewart, L. Edwards, J. Santisteban, *ASME Journal of Tribology* 129 (2) (2007) 411–418.
- [21] H. Ito, R. Nakamura, M. Shiroyoma, T. Sasaki, *Post-treatment of plasma sprayed WC–Co coatings by hot isostatic pressing*, NTSC CA, 1990, pp. 233–238.

- [22] K.A. Khor, N.L. Loh, *Journal of Thermal Spraying* 3 (1) (1994) 57–62.
- [23] H. Kuribayashi, K. Suganuma, Y. Miyamoto, M. Koizumi, *American Ceramic Society Bulletin* 65 (9) (1986) 1306–1310.
- [24] V. Stoica, R. Ahmed, M. Golshan, S. Tobe, *Journal of Thermal Spray Technology* 13 (1) (2004) 93–107.
- [25] S. Stewart, R. Ahmed, T. Itsukaichi, *Wear* 257 (2004) 962–983.
- [26] J.A. Dann, M.R. Daymond, L. Edwards, J.A. James, J.R. Santisteban, *Physica B: Condensed Matter* 350 (2004) E511–E514.
- [27] M.W. Johnson, L. Edwards, P.J. Withers, *Physica B* 234 (1997) 1141–1143.
- [28] L. Edwards, in: M.E. Fitzpatrick, A. Lodini (Eds.), *Analysis of Residual Stress by Diffraction using Neutron and Synchrotron Radiation*, Taylor and Francis, London, 2003, pp. 233–248.
- [29] D. Wang, L. Edwards, in: S. Denis et al. (Eds.), *Proceedings of the Fourth European Conference on Residual Stresses, Société Française de Métallurgie et de Matériaux*, vol. 1, 1998, pp. 135–144.
- [30] D. Wang, I.B. Harris, P.J. Withers, L. Edwards, in: S. Denis (Eds.), *Proceedings of the Fourth European Conference on Residual Stresses, Société Française de Métallurgie et de Matériaux*, vol. 1, 1998, pp. 69–78.
- [31] T. Lorentzen, *Journal of Neutron Research* 5 (1997) 167–180.
- [32] S. Spooner, X.L. Wang, *Journal of Applied Crystallography* 30 (4) (1997) 449–455.
- [33] X.L. Wang, S. Spooner, C.R. Hubbard, *Journal of Applied Crystallography* 31 (1998) 52–59.
- [34] C.R. Borlado, F.J. Mompean, R.L. Peng, *Journal of Applied Crystallography* 34 (5) (2001) 613–624.
- [35] M.J. Balart, A. Bouzina, M.E. Fitzpatrick, L. Edwards, *Materials Science and Engineering* 367 (2004) 132–142.
- [36] M. Buchmann, M. Escibano, R. Gadow, G. Burkle, in: C.C. Berndt (Ed.), *Thermal Spray: Surface Engineering via Applied Research*, ASM International, ISBN: 0-87170-680-6, 2002, pp. 598–605.
- [37] L. Powlaski, *The Science and Engineering of Thermal Spray Coatings*, ISBN 0-471-95253-2, 1995.
- [38] A to Z of Materials–azom (<http://www.azom.com/details.asp?ArticleID=133>).
- [39] H.L. Lovelock, *Journal of Thermal Spray Technology* 7 (3) (1998) 357–373.
- [40] C. Verdon, A. Karimi, J.L. Martin, *Materials Science and Engineering A* A246 (1998) 11–24.
- [41] J. Nerz, B. Kushner, A. Rotolico, *Journal of Thermal Spray Technology* 1 (2) (1992) 155–160.
- [42] B. Meredith, D.R. Milner, *Powder Metallurgy* 1 (1976) 38.
- [43] H.S. Ryoo, S.K. Hwang, B.K. Kim, H.S. Chun, *Metallurgical and Materials Transactions-A* 31A (2000) 1925–1935.
- [44] V. Stoica, *Sliding wear of post-treated thermal spray coatings*, PhD Thesis, School of EPS, Heriot-Watt University, Edinburgh, UK, 2005.
- [45] H. Nakahira, K. Miyajima, Y. Harada, *Proceedings of the ITSC, Thermal Spray Coatings: Research Design and Applications*, Orlando, USA, 1992, pp. 1011–1017.
- [46] S. Guo, Y. Kagawa, *Scripta Materiala* 50 (2004) 1401–1406.
- [47] Shipley, Becker, *Failure Analysis and Prevention*, ASM Handbook, vol. 11, Section 6E, ISBN 0-87170-704-7, 2002.
- [48] R. Ahmed, M. Hadfield, *Journal of Thermal Spray Technology* 11 (3) (2002) 333–349.